1    **ORP1L regulates dynein clustering on endolysosmal membranes in response to**
2    **cholesterol levels**

3    Shreyasi Thakur[1], Peter K. Relich[1], Elena M. Sorokina[1], Melina T. Gyparaki[2], Melike

4    Lakadamyali[1,3,*]

5    [1] Department of Physiology, Perelman School of Medicine, University of Pennsylvania

6    [2] Department of Biology, School of Arts and Sciences, University of Pennsylvania

7    [3] Department of Cell and Developmental Biology, Perelman School of Medicine, University of

8    Pennsylvania

9    [*] Correspondence should be sent to: melikel@pennmedicine.upenn.edu

10   **Abstract**

11   The sub-cellular positioning of endolysosomes is crucial for regulating their function. Particularly,

12   the positioning of endolysosomes between the cell periphery versus the peri-nuclear region

13   impacts autophagy, mTOR (mechanistic target of rapamycin) signaling and other processes. The

14   mechanisms that regulate the positioning of endolysosomes at these two locations are still being

15   uncovered. Here, using super-resolution microscopy, we show that the retrograde motor dynein

16   forms nano-clusters on endolysosomal membranes containing 1-4 dyneins. Surprisingly, dynein

17   nano-clusters are larger on peripheral endolysosomes having higher cholesterol levels compared

18   to peri-nuclear ones. By perturbing endolysosomal membrane cholesterol levels, we show that

19   dynein copy number within nano-clusters directly depends on the amount of endolysosomal

20   cholesterol. Finally, we show that the dynein adapter protein ORP1L (Oxysterol Binding Protein

21   Homologue) regulates dynein clustering in response to cholesterol levels. Our work reveals a new

22   mechanism by which endolysosomal positioning is regulated through the cholesterol dependent

23   nano-organization of ORP1L and dynein.

24

25

## Introduction

Late endosomes, lysosomes and autolysosomes constitute a broad class of sub-cellular compartments (Klumperman and Raposo, 2014; Wijdeven et al., 2016) that we will refer to here as endolysosomes for simplicity. These compartments play key cellular roles including transport of cellular proteins destined for degradation, metabolic sensing, membrane repair and signaling (Gould and Lippincott-Schwartz, 2009). The maturation level, fusion capacity with other sub-cellular compartments and downstream function of endolysosomes are regulated by their intracellular transport and sub-cellular positioning. For example, dispersal of lysosomes from the peri-nuclear region to the cell periphery increases their association with mTORC1 (mechanistic target of rapamycin complex 1) and leads to downregulation of autophagy (Kimura et al., 2008; Korolchuk and Rubinsztein, 2011; Korolchuk et al., 2011; Pu et al., 2016). The transport and subcellular positioning of endolysosomes are in turn regulated by a myriad of mechanisms (Maday et al., 2014) including motor activation (Elshenawy et al., 2020; Fu and Holzbaur, 2014; Fu et al., 2014), motor tug-of-war (Belyy et al., 2016; Hendricks et al., 2010; Soppina et al., 2009) and association of motors with microtubule tracks having distinct post-translational modifications (Guardia et al., 2016; Mohan et al., 2019; Nirschl et al., 2016).

Peripheral transport of endolysosomes is mediated by kinesin motors belonging to different kinesin families (Kif5, Kif1, Kif3) (Brown et al., 2005; Cardoso et al., 2009; Encalada et al., 2011; Mohan et al., 2019; Rosa-Ferreira and Munro, 2011), whereas dynein is responsible for their retrograde transport toward the perinuclear region (Granger et al., 2014; Reck-Peterson et al., 2018). Recent discovery of dynein activating adapters have revolutionized our understanding of how dynein mediates efficient retrograde transport (Elshenawy et al., 2020; McKenney et al., 2014; Olenick and Holzbaur, 2019; Reck-Peterson et al., 2018; Schroeder and Vale, 2016). Dynein assembles into an autoinhibitory, weakly processive conformation, while dynein activating adaptors are crucial for dynein's assembly with dynactin and the processive motility of the dynein-dynactin complex on microtubules (Chowdhury et al., 2015; McKenney et al., 2014; Schroeder and Vale, 2016; Urnavicius et al., 2018). Recent Cryo-EM studies showed that certain early endosomal dynein activating adapters including BICD2 and Hook3 recruit two dynein dimers (Urnavicius et al., 2018). *In vitro* assays further showed that these heteromeric dynein complexes move faster and navigate obstacles better compared to single dynein (Elshenawy et al., 2019; Ferro et al., 2019; Urnavicius et al., 2018). Hence, in addition to mediating dynein's interaction with dynactin and bringing dynein out of its auto-inhibitory confirmation, these activators further improve the efficiency of dynein mediated motility by allowing two copies of dynein to assemble

59    together into complexes. Yet, to date, the stoichiometry of adapter-dynein-dynactin complexes on

60    sub-cellular compartments i*n vivo* and how these complexes are spatially organized on the

61    membrane of sub-cellular compartments are not known.  Dynein is recruited to endolysosomal

62    compartments via the cholesterol-sensing tripartite complex Rab7-RILP-ORP1L (Johansson et

63    al., 2007; Pfeffer, 2001; Rocha et al., 2009). Whether this tripartite complex can recruit multiple

64    copies of dynein dimers to improve the efficiency of retrograde transport of endolysosomal

65    compartments in response to cellular cues is unknown.

66    Super-resolution is a powerful tool for studying spatial nano-organization of proteins within the

67    cell, yet, only a handful of studies have been carried out to date to visualize proteins on the

68    membrane of sub-cellular compartments (Franke et al., 2019; Puchner et al., 2013). Previously,

69    using super-resolution microscopy, we showed that dynein forms nano-clusters on microtubules

70    consisting of small teams of dynein motors (Cella Zanacchi et al., 2019; Zanacchi et al., 2017a).

71    However, whether these nano-clusters are formed on the membrane of endolysosomes, the

72    mechanisms of nano-cluster formation and whether formation of larger nano-clusters containing

73    more dynein motors lead to more efficient retrograde transport are not known. Here, using

74    quantitative super-resolution microscopy, we show that dynein forms nano-clusters on

75    endolysosomes, consisting of 1-4 dyneins. Our data suggest that for efficient retrograde transport,

76    dynein should be present in multiples of two copies within nano-clusters (e.g. 4 dyneins). The

77    copy number of dynein within nano-clusters is in turn regulated by membrane cholesterol levels

78    and ORP1-L's cholesterol sensing domain.

79

80    **Results**

81    **Dynein forms nano-clusters on endolysosomes containing 1-4 dynein motors with a switch**

82    **to larger nano-clusters on peripheral versus peri-nuclear endolysosomes.**

83    To visualize the spatial organization of dynein on endolysosomal membranes we expressed

84    mCherry-ORP1L in HeLa cells in which endogenous ORP1L was targeted by CRISPR/Cas9

85    mutagenesis (ORP1L-KO)(Zhao and Ridgway, 2017). The mCherry-ORP1L signal substantially

86    overlapped with that of CD63, an endolysosomal marker (Beatty, 2006; van der Kant et al., 2013;

87    Vanlandingham and Ceresa, 2009), indicating that ORP1L marks endolysosomes (Figure 1--

88    figure supplement 1A). Hence, we took mCherry-ORP1L positive sub-compartments in the wide-

89    field images that were isolated, round and diffraction limited in size (200-500 nm FWHM) as an

90    endolysosome for further analysis (Figure 1A and Figure 1--figure supplement 1B). To determine

91    whether dynein was clustered on these endolysosomes, we carried out super-resolution imaging

92    of dynein labeled with an antibody against the dynein intermediate chain (IC74). These images

93    revealed nano-clusters within the cell cytoplasm similar to what we have previously demonstrated

94    (Cella Zanacchi et al., 2019) (Figure 1A-B). We manually cropped the central intensity peak of

95    mCherry-ORP1L positive endolysosomes (Figure 1--figure supplement 1B and Methods) and

96    used it as a mask in the super-resolution image to specifically segment dynein nano-clusters that

97    overlapped with an endolysosomal compartment (Figure 1A-B). Dynein super-resolution images

98    were further segmented into individual nano-clusters using a previously developed Voronoi

99    tessellation approach (Figure 1--figure supplement 1C) (Levet et al., 2015). We then quantified

100   the number of localizations per dynein nano-cluster for peripherally- and peri-nuclearly-positioned

101   endolysosomes (Figure 1C). The peripheral and peri-nuclear endolysosomes were separated

102   manually based on their proximity to the cell nucleus (Figure 1--figure supplement 1D). The

103   number of localizations per nano-cluster is proportional to the nano-cluster size as well as to the

104   copy number of dynein within nano-clusters (Cella Zanacchi et al., 2019; Zanacchi et al., 2017a).

105   Surprisingly, we found that the dynein nano-clusters associated to peripheral endolysosomes

106   contained a significantly higher number of localizations compared to peri-nuclear endolysosomes

107   (mean = 67±1.9 for peripheral and 54±1.8 for perinuclear endolysosomes) (Figure 1C).

108
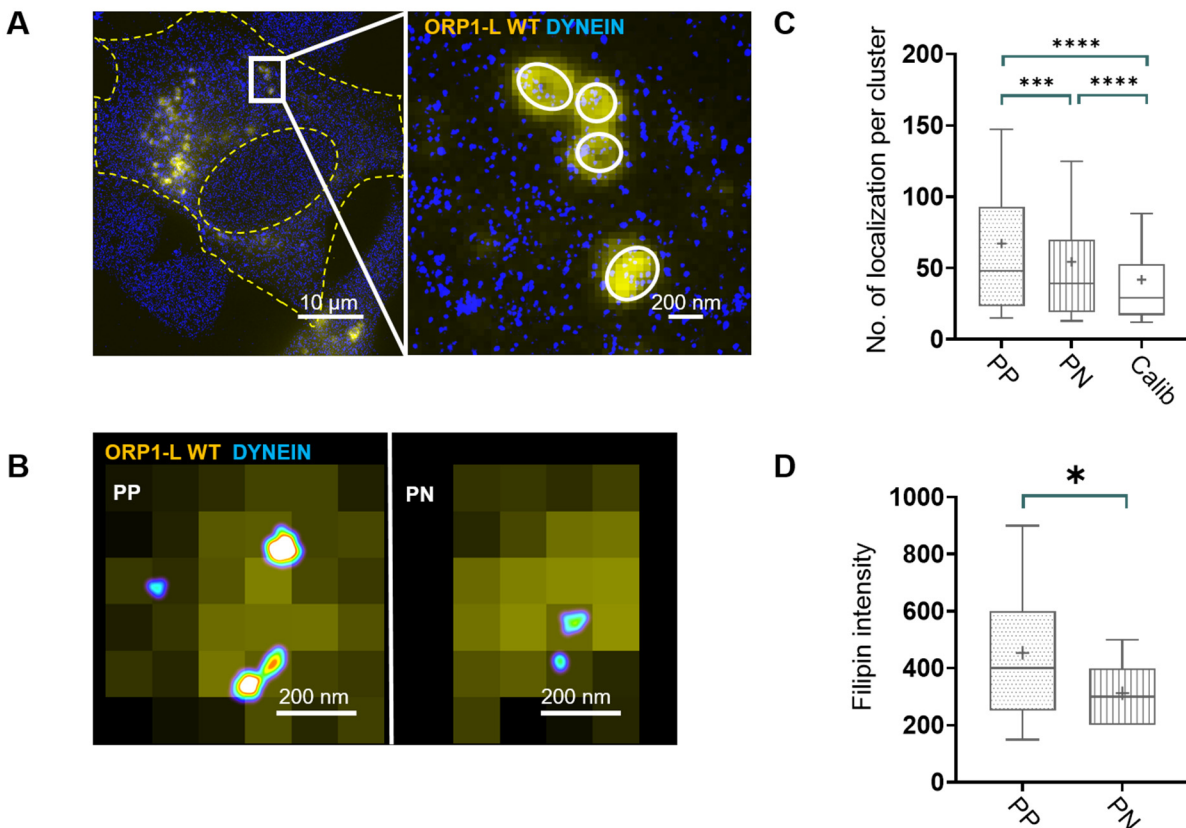
*Figure 1: Dynein forms larger nano-clusters containing a higher proportion of dynein multimers on endolysosomes positioned at the cell periphery:*

*(A) Cropped wide-field image of cells expressing full length ORP1L fused to mCherry (mCherry-ORP1L-WT, yellow) overlaid with super-resolution image of dynein (blue). Cell edge and nucleus are highlighted in yellow dashed lines. A zoom of the white rectangle is shown in which mCherry-ORP1L-WT positive endolysosomes are highlighted with white circles.*

*(B) An overlay of wide-field image of ORP1L (yellow) and super-resolution image of dynein (image is color coded according to localization density with higher density corresponding to white and lower density corresponding to cyan) for an endolysosome positioned at the cell periphery (PP) and peri-nuclear region (PN).*

*(C) Box plot showing the number of localizations per dynein nano-cluster for peripherally positioned endolysosomes (PP) (n=195 endolysosomes from n=6 cells, n=2experiments, mean 67±1.9), peri-nuclearly positioned endolysosomes (PN) (n=210 endolysosomes from n=6 cells, n=2 experiments, mean 54±1.8) and in cells in which dynein has been*

124 *labeled with a 100-fold dilution of the primary antibody for sparsely labeling single dynein*

125 *motors (n=6 cells, n=1 experiments, see methods, mean 42±0.2). The box corresponds*

126 *to 25-75 percentile, the line corresponds to the median, the cross corresponds to the*

127 *mean, and the whiskers correspond to 10-90 percentile. Statistical significance was*

128 *assessed using a Kolmogorov-Smirnov-test with a p-value of. ***: 0.001, ****: <0.0001.*

129 *(D) Box plot showing the intensity of filipin, which binds cholesterol, on peripherally positioned*

130 *endolysosomes (PP) (n=44 endolysosomes from n=4 cells, n=2 experiments, mean*

131 *454±40) versus peri-nuclearly positioned endolysosomes (PN) (n=41 endolysosomes*

132 *from n=5 cells, n=2 experiments, mean 312±19). The box corresponds to 25-75 percentile,*

133 *the line corresponds to the median, the cross corresponds to the mean and the whiskers*

134 *correspond to 10-90 percentile. Statistical significance was assessed using a Kolmogorov-*

135 *Smirnov-test with a p-value of 0.02*

136 To obtain a quantitative estimate of the copy number of dynein within nano-clusters, we carried

137 out a calibration experiment in which we diluted the primary antibody by 100-fold, aiming to

138 sparsely label single copies of dynein (Ehmann et al., 2014) (Figure 1--figure supplement 1E and

139 Methods).  We then used the number of localizations per dynein nano-cluster in these sparse

140 labeling experiments as a calibration corresponding to a single dynein motor (Figure 1C, Figure

141 1--figure supplement 1F). We previously showed that fitting the distribution of the number of

142 localizations per nano-cluster to a linear convolution of monomeric calibration functions enables

143 estimation of the copy number composition of a protein of interest in super-resolution images

144 (Zanacchi et al., 2017b). Using this approach, we estimated that nano-clusters on peri-nuclear

145 endolysosomes mainly consist of 1-2 copies of dynein motor (74% single, 11% 2, 7% 3 and 8%

146 4 copies) (Figure 1--figure supplement 1F). Interestingly, on peripheral endolysosomes the

147 proportion of nano-clusters containing 1-2 dynein motors decreased and the proportion of nano-

148 clusters containing 3-4 motors increased (70% single, 2% 2, 9% 3 and 18% 4 copies of dynein

149 (Figure 1--figure supplement 1F). In particular, there was a 2-fold increase in the proportion of

150 nano-clusters with 4 copies of dynein on peripheral endolysosomes. We next asked if the

151 membrane cholesterol content may be responsible for the increased dynein clustering and the

152 switch from primarily 1-2 copies of dynein to increased 3-4 copies of dynein on peripheral

153 endolysosomes. To start addressing this question, we measured the cholesterol levels of

154 peripheral and peri-nuclear endolysosomes by labeling mCherry-ORP1L expressing HeLa cells

155 with filipin, a toxin that binds cholesterol. We measured the filipin intensity on mCherry-ORP1L

156 positive endolysosomes and found that membrane cholesterol levels of peripheral

157 endolysosomes were indeed higher compared to peri-nculear endolysosomes (Figure 1D). These

6

158 results indicate a correlation between endolysosomal membrane cholesterol levels,
159 endolysosomal positioning and dynein clustering.

160

161 **Membrane cholesterol levels determine the level of dynein clustering and dynein copy**
162 **number within nano-clusters on endolysosomes.**

163 It is known that positioning of endolysosomal compartments in the cell affects their membrane
164 composition, maturation and signaling (Cabukusta and Neefjes, 2018; Hu et al., 2015; Hyttinen
165 et al., 2013). To better understand the mechanisms behind dynein clustering and to causally relate
166 dynein clustering to endolysosomal membrane cholesterol levels, we manipulated cholesterol
167 levels with two commonly used drugs: U18666A that increases endolysosomal membrane
168 cholesterol and Lovastatin that decreases cellular and endolysosomal membrane cholesterol
169 levels (Keyomarsi, 1996; Rocha et al., 2009). mCherry-ORP1L-positive endolysosomes in
170 ORP1L KO HeLa cells treated with U18666A indeed had higher membrane cholesterol levels (by
171 4.5-fold) compared to those in cells treated with lovastatin as measured by filipin intensity (Figure
172 2--figure supplement 1A). We will refer to the endolysosomal membrane cholesterol content of
173 the U18666A and Lovastatin treated cells as 'high cholesterol' and 'low cholesterol' condition,
174 respectively.

175 Super-resolution imaging revealed that dynein nano-clusters on endolysosomal compartments
176 contained a significantly higher number of localizations under high cholesterol compared to low
177 cholesterol conditions (mean = 71±1.9 for high and 50±1.9 for low cholesterol) (Figure 2A-B).

178
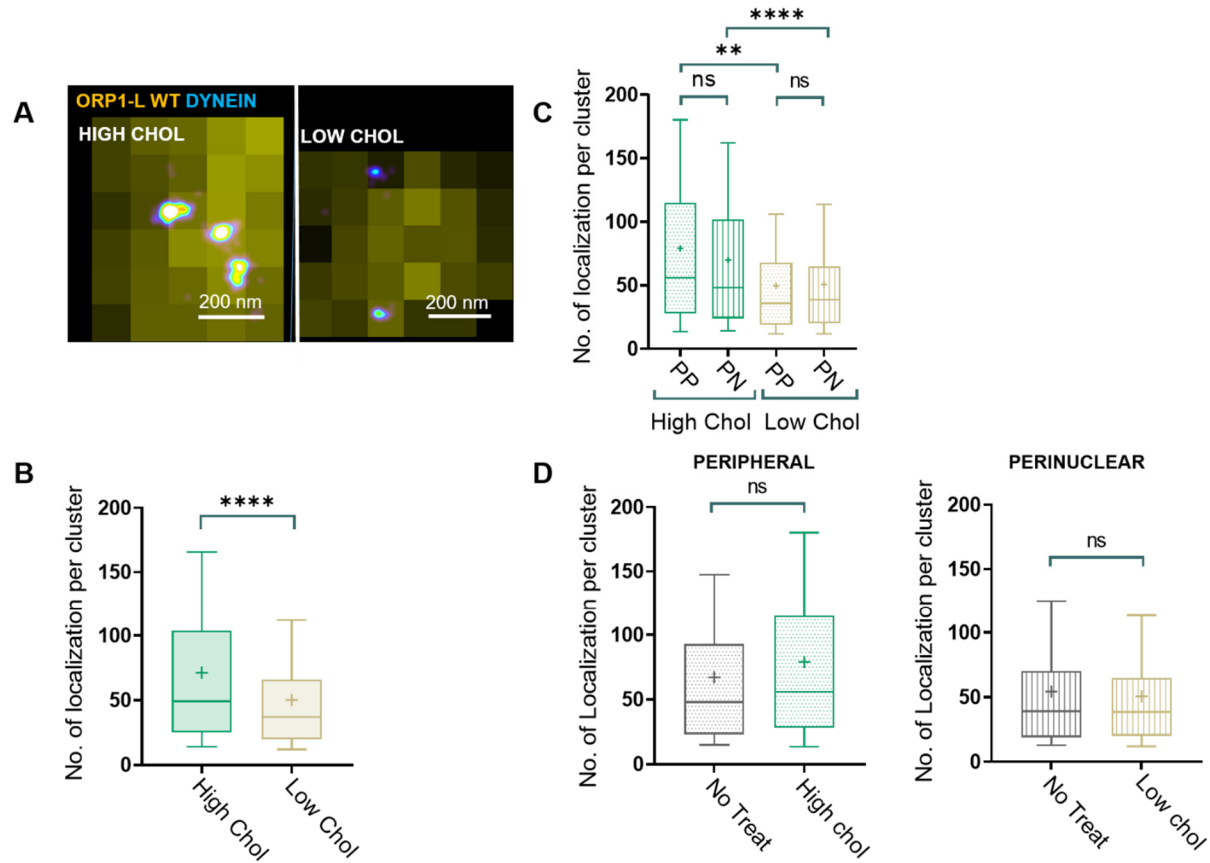
*Figure 2: Dynein forms larger nano-clusters containing a higher proportion of dynein multimers on endolysosomes that have high cholesterol content compared to those that have low cholesterol content:*

*(A) An overlay of cropped wide-field image of ORP1L (yellow) and super-resolution image of dynein (image is color coded according to localization density with higher density corresponding to white and lower density corresponding to cyan) for an endolysosome in cells treated with U18666A (High Chol) or Lovastatin (Low Chol).*

*(B) Box plot showing the number of localizations per dynein nano-cluster for endolysosomes in U18666A treated cells (High Chol) (n=224 endolysosomes from n=6 cells, n=2 experiments, mean 71±1.9) versus Lovastatin treated cells (Low Chol) (n=217 endolysosomes from n=6 cells, n=2 experiments, mean 50±1.9). The box corresponds to 25-75 percentile, the line corresponds to the median, the cross corresponds to the mean and the whiskers correspond to 10-90 percentile. Statistical significance was assessed using a Kolmogorov-Smirnov-test with a p-value <0.0001.*

8

193     *(C) Box plot showing the number of localizations per dynein nano-cluster for peripherally*
194     *positioned (n=70 endolysosomes from n=6 cells, n=2 experiments, mean 79±5) or peri-*
195     *nuclearly positioned (n=154 endolysosomes from n=6 cells, n=2 experiments, mean 70±2)*
196     *endolysosomes in U18666A treated cells (High Chol PP and High Chol PN, respectively)*
197     *or Lovastatin treated cells (Low Chol PP; n=110endolysosomes from n=6 cells, n=2*
198     *experiments, mean 50±2.7 and Low Chol PN; n=107 endolysosomes from n=6 cells, n=2*
199     *experiments, mean 51±2.8, respectively). The box corresponds to 25-75 percentile, the*
200     *line corresponds to the median, the cross corresponds to the mean and the whiskers*
201     *correspond to 10-90 percentile. Statistical significance was assessed using a Kolmogorov-*
202     *Smirnov-test with a p-value of n.s.: 0.27, n.s.: 0.93, \*\*: 0.001, \*\*\*\*: <0.0001.*

203     *(D) Box plot showing the number of localizations per dynein nano-cluster for peripherally*
204     *positioned endolysosomes in untreated cells (No Treat) (n=195 endolysosomes from n=6*
205     *cells, n=2 experiments, mean 67±1.9) and U18666A treated cells (High Chol) (n=70*
206     *endolysosomes from n=6 cells, n=2 experiments, mean 79±5); as well as in perinuclearly*
207     *positioned endolysosomes in untreated cells (No Treat) (n=210 endolysosomes from n=6*
208     *cells, n=2 experiments, mean 54±1.8) and Lovastatin treated cells (Low Chol) (n=107*
209     *endolysosomes from n=6 cells, n=2 experiments, mean 51±2.8). The box corresponds to*
210     *25-75 percentile, the line corresponds to the median, the cross corresponds to the mean*
211     *and the whiskers correspond to 10-90 percentile. Statistical significance was assessed*
212     *using a Kolmogorov-Smirnov-test with a p-value of 0.1353 and 0.7.*

213 These differences were not due to an increase in dynein expression level upon high cholesterol
214 drug treatment, as western blot analysis showed that the level of dynein expression did not
215 increase under high cholesterol treatment (Figure 2--figure supplement 1B). We fit the number of
216 localizations per nano-cluster distribution to the calibration data to determine dynein copy number
217 within nano-clusters under high and low cholesterol conditions (Figure 2--figure supplement 1C).
218 This analysis showed that dynein nano-clusters change from containing mainly single dynein
219 motors to containing an increased proportion of dynein multimers (75% single, 9% 2, 13% 3 and
220 3% 4 copies of dynein under low cholesterol conditions and 58% single, 13% 2, 1.2% 3 and 27%
221 4 copies of dynein under high cholesterol conditions) (Figure 2--figure supplement 1C).
222 Interestingly, there was a dramatic increase in the proportion of nano-clusters containing 4 copies
223 of dynein (9-fold) similar to the observations for peripheral versus peri-nuclear endolysosomes.
224 Finally, low cholesterol levels also led to an increase in the percentage of endolysosomes that
225 completely lacked dynein (Figure 2--figure supplement 1D, Low chol: 55%, High Chol: 27%).

226 We next analyzed the cholesterol levels of and dynein nano-cluster size on peripheral and peri-
227 nuclear endolysosomes under the two cholesterol treatment conditions. In contrast to
228 physiological conditions, peripheral and peri-nuclear endolysosomes had similar cholesterol
229 levels (Figure 2--figure supplement 1E) and similar dynein clustering under both high and low
230 cholesterol conditions  (High cholesterol: mean = 79±9 and 70±2 localizations per cluster for
231 peripheral and peri-nuclear endolysosomes, respectively and Low Cholesterol: mean = 50±2.7
232 and 51±2.8 localizations per cluster for peripheral and peri-nuclear endolysosomes, respectively)
233 (Figure 2C). Interestingly, the dynein clustering level of peri-nuclear endolysosomes under
234 physiological conditions (mean = 54±1.8 localizations per cluster) was similar to those under low
235 cholesterol conditions (mean = 51±1.8 localizations per cluster) and the dynein clustering level of
236 peripheral endolysosomes under physiological conditions (mean = 67±1.9 localizations per
237 cluster) was similar to those under high cholesterol conditions (mean = 79±5 localizations per
238 cluster) (Figure 2D). These results indicate that cholesterol levels and not endolysosome
239 positioning determine the level of dynein clustering on endolysosomal membranes. Finally, the
240 positioning of endolysosomes was impacted by cholesterol levels, with low cholesterol leading to
241 more scattered and high cholesterol leading to more peri-nuclearly positioned endolysosomes
242 (Figure 2--figure supplement 1F), consistent with previous results (Rocha et al., 2009).

243 Taken together our results show that membrane cholesterol levels impact not only dynein
244 recruitment but importantly also the level of dynein clustering and the proportion of dynein
245 multimers on endolysosomal membranes, impacting the balance between antero- and retro-grade
246 transport of these compartments and leading to their re-positioning with respect to the cell peri-
247 nuclear region.

248

249 **The cholesterol sensing domain of ORP1L regulates ORP1L clustering on endolysosomal**
250 **membranes in a cholesterol dependent manner.**

251 Dynein does not bind directly to endolysosomal membranes and the mechanisms that can lead
252 to the formation of larger dynein nano-clusters with increased number of dynein motors in them
253 are unknown. Dynein is recruited to endolysosomes through a tripartite complex of Rab7-ORP1L-
254 RILP (Johansson et al., 2007; Pfeffer, 2001; Rocha et al., 2009). ORP1L contains multiple lipid
255 binding domains that allow it to bind to either oxysterols or phospholipids (Johansson et al., 2005;
256 Olkkonen and Li, 2013; Zhao and Ridgway, 2017). Hence, we asked whether the cholesterol
257 sensing domain of ORP1L is responsible for regulating dynein clustering on endolysosomal

258 membranes. To address this question, we first imaged ORP1L's spatial distribution on
259 endolysosomes in wild type or ORP1L-KO HeLa cells that express mCherry-ORP1L (Zhao and
260 Ridgway, 2017) under low or high cholesterol treatment conditions using super-resolution
261 microscopy (Figure 3A). We again analyzed isolated, round mCherry-ORP1L positive
262 endolysosomes within a size range of 50-500 nm in the super-resolution images. ORP1L
263 appeared uniformly distributed on the endolysosomal membrane under low cholesterol conditions
264 and more clustered under high cholesterol conditions (Figure 3A).
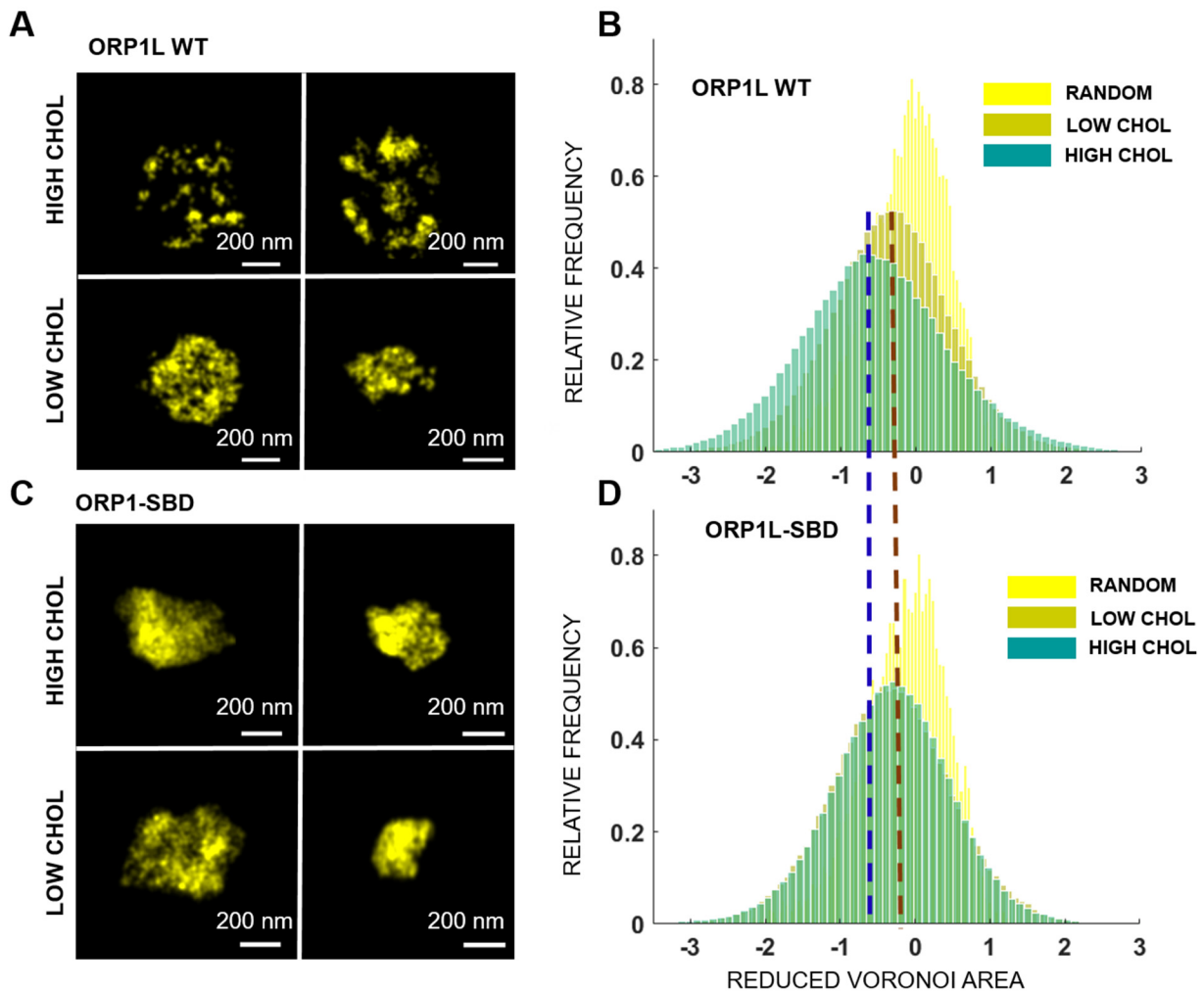


265

266 *Figure 3: ORP1L is more clustered on endolysosomes having higher cholesterol levels in a*
267 *manner dependent on its cholesterol binding domain:*

268 *(A) Super-resolution images of full length ORP1L (mCherry-ORP1L-WT) in cells treated with*
269 *U18666A (High Chol, upper panels) and in cells treated with Lovastatin (Low Chol, lower*
270 *panels).*

271    *(B) Log plot of the Reduced Voronoi Polygon area distribution for super-resolution images of*

272    *full length ORP1L (mCherry-ORP1L-WT) in cells treated with U18666A (dark green, High*

273    *Chol) (n=95 endolysosomes from n=6 cells, n=2 experiments), Lovastatin (light green,*

274    *Low Chol) (n=107 endolysosomes from n=6 cells, n=2 experiments) and for a random*

275    *distribution of localizations (yellow, Random). The dashed lines are a guide to the eye to*

276    *highlight the shift in the peak position of Reduced Voronoi Polygon area distributions with*

277    *cholesterol treatment for full length ORP1L (mCherry-ORP1L-WT) and sterol binding*

278    *deficient ORP1L mutant lacking residues 560-563 (mCherry-ORP1L-SBD).*

279    *(C) Super-resolution images of sterol binding deficient ORP1L mutant lacking residues 560-*

280    *563 (mCherry-ORP1L-SBD) in cells treated with U18666A (High Chol, upper panels) and*

281    *in cells treated with Lovastatin (Low Chol, lower panels).*

282    *(D) Log plot of the Reduced Voronoi Polygon area distribution for super-resolution images of*

283    *sterol binding deficient ORP1L mutant lacking residues 560-563 (mCherry-ORP1L-SBD)*

284    *in cells treated with U18666A (dark green, High Chol) (n=120 endolysosomes from n=6*

285    *cells, n=2 experiments), Lovastatin (light green, Low Chol) (n=170 endolysosomes from*

286    *n=6 cells, n=2 experiments) and for a random distribution of localizations (yellow,*

287    *Random).*

288    To quantify the level of ORP1L clustering, we once again used Voronoi tessellation to segment

289    individual ORP1L clusters on endolysosomal membranes. This approach revealed an increased

290    number of ORP1L clusters under high cholesterol (mean = 2.6±0.32 clusters per endolysosome)

291    compared to low cholesterol (mean = 1±0.04 clusters per endolysosome) conditions (Figure 3--

292    figure supplement 1A). However, we also found that, surprisingly, the localization density of

293    ORP1L was higher on endolysosomes under low compared to high cholesterol conditions (Figure

294    3--figure supplement 1B), suggesting that more ORP1L binds to endolysosomes when their

295    membrane cholesterol levels are lower. To ensure that the increased protein density does not

296    confound the clustering analysis using Voronoi tessellation, which is dependent on localization

297    density, we developed an alternative quantification method that is insensitive to differences in

298    localization density and protein amount (Methods). To this end, we carried out Voronoi tessellation

299    and re-scaled the distribution of Voronoi polygon areas so that the mean area was set to unity.

300    We refer to the re-scaled quantities as reduced areas.  The distribution of reduced areas provides

301    a means to measure the clustering tendency of ORP1L from various conditions without explicitly

302    compensating for different localization densities.  For a clustered distribution, we expected to see

303    a shift in the mode of the reduced Voronoi polygon area distribution towards a smaller value.

304    Indeed, the mode of the distribution for endolysosomal compartments under high cholesterol

12

305     conditions was shifted to smaller polygon areas compared to low cholesterol conditions or
306     compared to a simulated random distribution, indicating that ORP1L is more clustered on
307     endolysosomes with high membrane cholesterol levels (Figure 3B). We further used a statistical
308     test (Kullback-Leibler Divergence or KL Divergence) to determine how much the ORP1L
309     organization differed from a random distribution under low and high cholesterol conditions. The
310     difference from the normalized random distribution of points to the experimental distribution, which
311     we call the clustering tendency score, was 0.75 under high cholesterol and 0.14 under low
312     cholesterol (a 5-fold difference). These results further confirm that ORP1L's organization on
313     endolysosomal membranes deviated significantly more from a random distribution under high
314     cholesterol compared to low cholesterol conditions. When endogenous ORP1L on CD63 positive
315     endolysosomal compartments was imaged in wild type HeLa cells using an ORP1L antibody, it
316     also was more clustered and had lower localization density under high cholesterol compared to
317     low cholesterol conditions (Figure 3--figure supplement 1C-D), demonstrating that the results are
318     not an artifact of ORP1L over-expression. Overall, these super-resolution data show that ORP1L,
319     like dynein, is more clustered on endolysosomes having higher membrane cholesterol levels.

320     To determine if the differences in ORP1L's spatial distribution on endolysosomes were due to its
321     cholesterol binding, we expressed mCherry fused to a sterol binding deficient ORP1L mutant
322     lacking the residues 560–563 (mCherry-ORP1L-SBD) (Vihervaara et al., 2011; Zhao and
323     Ridgway, 2017) in HeLa ORP1L KO cells (Figure 3C-D and Figure 3--figure supplement 1E-F).
324     Super-resolution images of the mCherry-ORP1L-SBD mutant (Figure 3C) and both Voronoi
325     cluster segmentation (Figure 3--figure supplement 1E) and reduced Voronoi polygon area
326     distribution analysis (Figure 3D) (Clustering tendency score for ORP1L-SBD: 0.1 for high and
327     0.09 for low cholesterol conditions) showed that the distribution of the ORP1L-SBD mutant was
328     uniform on endolysosomal membranes independent of cholesterol levels. The membrane
329     localization density of this mutant was overall high under both high and low cholesterol conditions
330     (Figure 3--figure supplement 1F) and at a similar level to the full length ORP1L under low
331     cholesterol conditions (Figure 3--figure supplement 1B). These results suggest that under low
332     cholesterol or when ORP1L lacks its cholesterol sensing domain, it is recruited to and binds
333     phospholipids on endolysosomes at a high level and likely in a non-specific manner. Finally, under
334     physiological conditions (no cholesterol treatment) the full-length ORP1L was more clustered on
335     peripherally positioned endolysosomes that have higher cholesterol levels whereas these
336     differences in ORP1L clustering were absent for the ORP1L-SBD mutant (Figure 4--figure
337     supplement 1A-B).

13

338    Overall, these results strongly support that the cholesterol sensing domain of ORP1L regulates

339    its spatial distribution on endolysosomal membranes in a cholesterol dependent manner, with

340    high cholesterol leading to more specific ORP1L recruitment (Figure 3--figure supplement 1B)

341    and a clustered ORP1L spatial organization (Figure 3A-B).

342

343

344    **The cholesterol sensing domain of ORP1L regulates dynein clustering and endolysosomal**

345    **positioning in a cholesterol dependent manner.**

346    Having established that ORP1L's cholesterol sensing domain regulates ORP1L's level of

347    clustering on endolysosomal membranes in a cholesterol dependent manner, we next asked if

348    ORP1L's spatial organization also impacts dynein clustering. We thus imaged dynein using super-

349    resolution microscopy in ORP1L-KO HeLa cells expressing the mCherry-ORP1L-SBD mutant.

350    Analysis of dynein nano-clusters on endolysosomes under high and low cholesterol conditions

351    showed that dynein clustering was no longer sensitive to cholesterol levels in cells expressing the

352    mCherry-ORP1L-SBD mutant as the sole ORP1L isoform (mean = $51\pm1.2$ for high and $53\pm0.88$

353    for low cholesterol) (Figure 4A-B). In addition, the level of dynein clustering in cells expressing

354    the mCherry-ORP1L-SBD mutant was similar to the level of dynein clustering under low

355    cholesterol conditions in cells expressing the full length mCherry-ORP1L (mean = $50\pm1.9$)

356    (compare Figure 2B and Figure 4B).

14

357
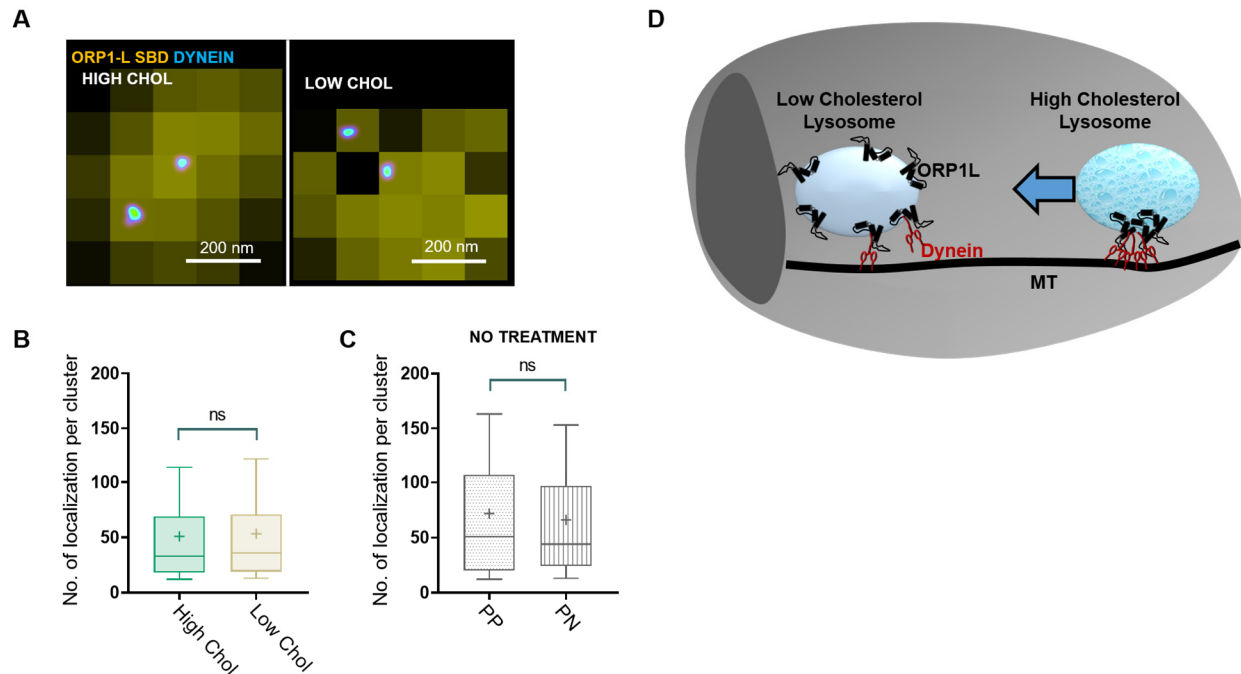
*Figure 4*: Dynein nano-clusters are insensitive to cholesterol levels in cells expressing sterol binding deficient ORP1L mutant:

*(A) An overlay of cropped wide-field image of ORP1L (yellow) and super-resolution image of dynein (image is color coded according to localization density with higher density corresponding to white and lower density corresponding to cyan) for an endolysosome in cells expressing sterol binding deficient ORP1L mutant lacking residues 560-563 (mCherry-ORP1L-SBD) and treated with U18666A (High Chol) or Lovastatin (Low Chol).*

*(B) Box plot showing the number of localizations per dynein nano-cluster for endolysosomes in cells expressing the sterol binding deficient ORP1L mutant lacking residues 560-563 (mCherry-ORP1L-SBD) and treated with U18666A (High Chol) (n=450 endolysosomes from n=6 cells, n=2 experiments, mean 51±1.2) versus Lovastatin (Low Chol) (n=300 endolysosomes from n=6 cells, n=2 experiments, mean 53±0.88). The box corresponds to 25-75 percentile, the line corresponds to the median, the cross corresponds to the mean and the whiskers correspond to 10-90 percentile. Statistical significance was assessed using a Kolmogorov-Smirnov-test with a p-value of 0.06.*

*(C) Box plot showing the number of localizations per dynein nano-cluster for peripherally positioned endolysosomes (n=100 endolysosomes from n=5 cells, n=2 experiments, mean 71±6) and peri-nuclearly positioned endolysosomes (n=150 endolysosomes from n=5 cells, n=2 experiments, mean 66±2) in cells expressing the sterol binding deficient*

15

377    *ORP1L mutant lacking residues 560-563 (mCherry-ORP1L-SBD). The box corresponds*
378    *to 25-75 percentile, the line corresponds to the median, the cross corresponds to the mean*
379    *and the whiskers correspond to 10-90 percentile. Statistical significance was assessed*
380    *using a Kolmogorov-Smirnov-test with a p-value of 0.44.*
381    *(D) Cartoon model showing how cholesterol levels and ORP1L regulate dynein nano-*
382    *clustering and endolysosome positioning. Peripheral lysosomes with higher cholesterol*
383    *content have a more clustered organization of ORP1L and dynein leading to efficient*
384    *retrograde transport (blue arrow). Perinuclear lysosomes having lower cholesterol content*
385    *have more uniform ORP1L organization leading to lower dynein recruitment and clustering*
386    *likely facilitating endolysosome anchoring at the peri-nuclear region or anterograde*
387    *trafficking back to the cell periphery.*

388    The sub-cellular positioning of endolysosomes also became insensitive to cholesterol treatment
389    in cells expressing the mCherry-ORP1L-SBD mutant and the endolysosomes were overall more
390    scattered throughout the cell under high or low cholesterol conditions as well as under
391    physiological conditions (Figure 4--figure supplement 1C). Finally, peripheral and peri-nuclear
392    endolysosomes had similar level of dynein clustering in untreated cells expressing the mCherry-
393    ORP1L-SBD mutant (mean = 71±6 localizations per cluster for high and 66±2 localizations per
394    cluster for low cholesterol) (Figure 4C). Taken together, these results show that the increased
395    clustering and higher copy number of dynein within nano-clusters on peripherally located
396    endolysosomes with higher cholesterol content is dependent on the cholesterol binding and
397    clustering ability of ORP1L (Figure 4D).

398

## Discussion

400    Here using super resolution microscopy and quantitative analysis, we visualize the spatial
401    organization of dynein motor and its adapter protein ORP1L on endolysosomal membranes. We
402    find that dynein forms nano-clusters consisting of mainly single but also a small but significant
403    proportion of multiple copies of dynein motor. Using perturbation experiments in which we
404    manipulated endolysosomal membrane cholesterol levels we show that the level of dynein
405    clustering and the copy number of dynein within nano-clusters on endolysosomal membrane is
406    increased under high cholesterol. This increased clustering is regulated by the cholesterol binding
407    ability of ORP1L that forms part of the Rab7-ORP1L-RILP tripartite complex, which recruits dynein
408    to endolysosomal membranes.

16

409    Cryo-EM experiments demonstrated that BICD2 and Hook3 bind two copies of dynein motors
410    (Urnavicius et al., 2018) but whether the endolysosomal adapter proteins Rab7-ORP1L-RILP also
411    recruit multiple dyneins is unknown. Our results demonstrate that besides the stoichiometry
412    between motor proteins and their adapter proteins, additional mechanisms inside cells are at play
413    to increase motor protein clustering and retrograde transport efficiency. We show that clustering
414    of adapter proteins into cholesterol enriched domains impacts the clustering of dynein motor on
415    endolysosomal membranes, increasing the efficiency of retrograde transport. High cholesterol
416    treatment increased the proportion of nano-clusters containing dynein multimers, with a big
417    increase on the proportion of nano-clusters containing 4 copies of dynein. Peripheral
418    endolysosomes also had a higher proportion of nano-clusters with 4 copies of dynein compared
419    to perinuclear endolysosomes. These results suggest that having dynein present in multiple
420    copies of two may be important for efficient retrograde transport, which is consistent with the
421    recent Cryo-EM and in vitro single molecule imaging data showing that coupled dyneins move
422    more processively and faster than single dynein (Urnavicius et al., 2018).

423    Previous *in vitro* work showed that early phagosomes engulfing 2-micron sized polystyrene beads
424    isolated from dictyostelium cells were completely uniformly covered with dynein on their
425    membrane whereas late phagosomes that move unidirectionally towards the retrograde direction
426    had a highly clustered dynein distribution (Rai et al., 2016). These changes in dynein distribution
427    were correlated to the membrane cholesterol content of phagosomes. In contrast, our results
428    show that instead of uniformly covering the entire membrane, only a small number of dyneins are
429    associated to endolysosomal membranes *in vivo.* A dramatic shift from a uniform dynein coverage
430    to a highly clustered dynein distribution hence is not needed for regulating retrograde transport of
431    native cellular compartments as these previous experiments with non-native compartments
432    suggested. Instead, a small shift from mainly single copies of dynein to a small proportion of
433    dynein mutimers (in particular containing 4 dyneins) is sufficient to bias retrograde transport of
434    native sub-cellular compartments.

435    Interestingly, the number of dyneins within nano-clusters is higher for peripherally located
436    endolysosomes, which also have higher cholesterol levels. Endolysosomes contact the
437    endoplasmic reticulum as they are trafficked within the cell cytoplasm (Friedman et al., 2013;
438    Rocha et al., 2009; Zhao and Ridgway, 2017). Such contacts lead to exchange of membrane
439    lipids and maturation of endolysosomes (van der Kant et al., 2013; Zhao and Ridgway, 2017). It
440    is plausible that multiple endolysosome-ER contacts during retrograde transport play a role in
441    lowering the cholesterol content of endolysosomes, leading to re-organization of ORP1L and

17

442  decreased dynein clustering. Hence, the peripheral endolysosomes with higher level of dynein
443  clustering are potentially those that are on their way to be retrogradely transported.  Future
444  correlative live-cell and super-resolution imaging experiments (Balint et al., 2013; Mohan et al.,
445  2019; Verdeny-Vilanova et al., 2017) will enable directly linking the transport properties of
446  endolysosomes to the level of dynein clustering on their membrane. Loss of membrane
447  cholesterol through ER contacts as these endolysosomes are retrogradely transported potentially
448  leads to loss of dynein clustering facilitating stalling/positioning at the perinuclear region or
449  anterograde trafficking back to the cell periphery via kinesin.

450  Previous studies showed that ORP1L, depending on its conformation, can either bind dynein or
451  make contacts with the ER-membrane (Olkkonen and Li, 2013; Rocha et al., 2009; Wijdeven et
452  al., 2016; Zhao and Ridgway, 2017). A change in ORP1L's conformation leads to shedding of
453  dynein and initiation of contact between ORP1L and the ER-membrane protein VAP to regulate
454  endolysosomal positioning (Rocha et al., 2009). Our results are consistent with these former
455  studies as we show that in addition to the level of dynein clustering, the recruitment of dynein to
456  endolysosomal compartments is also dependent on cholesterol levels. Under low cholesterol, the
457  percentage of endolysosomes completely lacking dynein was increased by ~2-fold (from 27% to
458  55%). However, around 45% of endolysosomes still contained dynein on their membrane even
459  under low cholesterol conditions. Here, we additionally show that ORP1L's nanoscale spatial
460  organization on the endolysosomal membranes is also dependent on cholesterol levels and
461  regulates dynein clustering, not only dynein recruitment. Hence, multiple mechanisms, including
462  recruitment of more dynein motors and clustering of the recruited dynein motors on the
463  endolysosomal membrane, are at play to increase the efficiency of retrograde transport and
464  regulate endolysosomal positioning. It will be interesting in the future to examine the differential
465  impact of having more dynein versus having dynein clustered in copies of two on the transport
466  and positioning of endolysosomes. It is plausible to hypothesize that increased dynein recruitment
467  in the absence of dynein clustering is not sufficient for enhancing retrograde transport.

468  Overall, our results provide an *in vivo* mechanism dependent on cholesterol levels by which
469  multiple dyneins can be recruited and clustered on endolysosomal membranes leading to their
470  efficient retrograde transport and positioning. Increased dynein clustering in response to
471  cholesterol levels is likely to be functionally significant as it impacts the sub-cellular positioning
472  of endolysosomal compartments. Metabolic disorders that lead to accumulation of lipids including
473  cholesterol in endolysosomal compartments like Niemann Pick Disease (NPC) are typically
474  associated with alterations in endolysosomal homeostasis and function (Torres et al., 2017). In

475  the future it would be interesting to explore if the nanoscale organization of ORP1L and dynein is

476  altered on endolysosomal membranes in NPC and other lysosomal storage disorders leading to

477  their mislocalization within the cell and whether restoring the proper nanoscale organization of

478  these cytoskeletal proteins can restore endolysosomal function. It would also be interesting to

479  determine if similar mechanisms play a role in regulating kinesin clustering or in regulating

480  transport of other organelles including Golgi vesicles and autophagosomes. It would further be

481  exciting to determine the precise stoichiometry of adapter-motor complexes on organelle

482  membranes to determine how the stoichiometry can be precisely tuned to regulate organelle

483  transport and positioning. Our work establishes the methodology needed and opens the door to

484  carry out these future studies.

485

486

487

488  **Materials and Methods**

489  **Cells and transfections**

490  Wild type HeLa cells were obtained from the American Type Culture Collection (CCL-2, ATCC,

491  Manassas, VA). HeLa-ORP1L-null cell lines, as well as mCherry-tagged ORP1L and ORP1L-

492  SBD constructs were a kind gift from Prof. Neale Ridgway (Dalhousie University, Depts. of

493  Pediatrics, and Biochemistry and Molecular Biology, Atlantic Research Centre, Halifax, Nova

494  Scotia, Canada). HeLa cells were grown in DMEM (GIBCO Laboratories, Grand Island, NY)

495  supplemented with 10% fetal bovine serum and antibiotics, and maintained in 5% $CO_2$ at

496  37°C. Cells were transiently transfected with mCherry-tagged wild type or mutant ORP1L at 70%

497  confluency using Lipofectamine 2000 reagent (Invitrogen) according to the manufacturer's

498  protocol. Cells were subjected to experimental treatments 24 h after transfection.

499  **Pharmacological treatment of cells**

500  Lovastatin (Sigma 1370600) was converted from its inactive prodrug form to its active open acid

501  form by dissolving Lovastatin (52gms) in ethanol (95%, 1.04 ml), followed by addition of 1N NaOH

502  (813 µl), followed by heating for 2 hrs at 50°C and neutralized with 1N HCL (pH 7.2). The volume

503  was made up to 13 ml by adding distilled water, giving 10mM active Lovastatin solution later

504  aliquoted and stored at -20°C(Keyomarsi, 1996). Mevalonic acid lactone (Sigma M4667, 1 gm)

505  was converted to its active form by dissolving in ethanol (3.5 ml), followed by addition of 1N NaOH

506  (4.2 ml ) and heating for 2 hrs at 55°C. The solution was made up to 15.4 ml with distilled water

507  and neutralized with 1N HCL (pH 7.2), giving 500 mM of stock solution, later aliquoted and stored

508  at -20. U18666A (Sigma U3633) was dissolved in ethanol giving final concentration of

509  10mg/ml(Rocha et al., 2009). For cholesterol depletion treatment, cells were cultured in DMEM,

510  10% Lipoprotein deficient serum (Sigma S5394), 50uM Lovastatin, 230uM Mevalonate for 6 hrs

511  before fixing for immunostaining. For high cholesterol treatment cells were cultured in DMEM,

512  10% FBS and 3μg/ml U18666A for 12 hrs before fixing.

**Immunostating**

514  Hela ORP1L KO cells were transiently transfected with ORP1L WT-mCherry or ORP1L SBD-

515  mCherry, treated with U18666A/Lovastatin or not treated and immunostained for ORP1L and

516  dynein. Endogenous ORP1L was immunostained in untransfected Hela cells treated with

517  U18666A/Lovastatin or not treated. For ORP1LWT/SBD-mCherry and endogenous ORP1L

518  immunostaning, cells were fixed with 4% (Vol/Vol) Paraformaldehyde in PBS for 20 mins and for

519  dynein immunostaining, cells were fixed in prechilled 1:1 Ethanol/Methanol solution for 3 mins on

520  ice.  The cells were blocked in blocking buffer (3% BSA, 0.2% Triton X-100 in PBS) for 1 hr. Cells

521  were incubated with primary anitbodies: Chicken anti-mCherry (Novus biotech nbp2-2515, 1:500)

522  ,mouse anti-dynein (Abcam ab23905, 1:50 or 1:5000 for single dynein imaging) and rabbit anti-

523  ORP1L (Abcam ab131165, 1:100) in blocking buffer for 1 hr on a rocker. Cells were washed with

524  washing buffer (0.2% blocking buffer, .05% Triton X-100 in PBS) three times. Custom made

525  secondary antibodies were labeled with an Alexa Fluor 405–Alexa Fluor A647 activator/reporter

526  dye pair combination at concentrations (0.1-0.15 mg/μl) and  used in the ratio of 1:50 in blocking

527  buffer for 40 mins, at RT on a rocker. Sample was then washed three times in PBS.

**Filipin staining**

529   Filipin (Sigma F4767) was lyophilized, aliquoted (250 μg per aliquot) and stored at -80°C. Filipin

530  was resuspended in 5 μl DMSO. Cells were fixed in 4% Paraformaldehyde for 20 mins and then

531  rinsed 3 times with PBS. Background autofluorescence was quenched with 50mM NH₄CL for 10

532  mins. Cells were incubated for 2 hrs with 100 μg/ ml working solution of Filipin in 3% BSA. Cells

533  were washed with 1% BSA in PBS three times before imaging. Imaging was performed

534  immediately.

**Western blot**

20

536    Western blot analysis was performed using the two-color Odyssey LI-COR (Lincoln, NE)
537    technique according to the manufacturer's protocol. A rabbit monoclonal antibody to ORP1L
538    (ab131165, Abcam), mouse monoclonal antibody to dynein (ab23905, Abcam), and a mouse
539    monoclonal antibody to detect GAPDH (clone 3B1E9, GenScript A01622–40) were used at a
540    dilution of 1:1,000 in blocking buffer. The secondary antibody IRDye800CW Donkey anti-Rabbit
541    and IRDye680RD Donkey anti-Mouse (LI-COR) were used in 1:10000 dilution for imaging in the
542    green 800-nm and red 700-nm channels, respectively.

543    **STORM Imaging**

544    Single-molecule imaging was done using imaging buffer comprising of 50 mM Tris, pH 7.5, 10
545    mM NaCl, 0.5 mg/mL glucose oxidase (Sigma, G2133), 40 µg/mL catalase (Roche Applied
546    Science, 106810), 10% (w/v) glucose and 10% (v/v) Ciseamine (77mg/ml of 360mM HCL) (Bates
547    et al., 2007). Images were acquired on the Oxford Nanoimager-S microscope which has the
548    following configuration: 405, 488, 561, and 640 nm lasers, 498–551 and 576–620 nm band-pass
549    filters in channel 1, and 665–705 nm band-pass filters in channel 2, 100× 1.4 NA objective
550    (Olympus), and a Hamamatsu Flash 4 V3 sCMOS camera. Localizations were acquired with 10-
551    ms exposure over 50,000 frames with 405 nm activation and 647 nm excitation. Images were
552    processed and localizations were obtained using the NimOS localization software (Oxford
553    Nanoimaging).

554    **Data Analysis**

555    To identify dynein clusters on ORP1L positive compartments, the intensity profile of conventional
556    ORP1L image was used as a mask. Line intensity profile of the ORP1L conventional image along
557    x and y axis was plotted on image J, and the width across one third of the full intensity maxima
558    was considered as the mask (*Figure 1*--figure supplement 1B). For the dynein calibration
559    experiments (100 fold diluted dynein antibody), dynein clusters were taken from the whole cell
560    except the nucleus region to avoid biased results.

561    For quantitative analysis we used custom written MATLAB codes. A previously described method
562    was adapted that segments super-resolution images based on Voronoi tessellation of the
563    fluorophore localizations (Andronov et al., 2016; Levet et al., 2015). Voronoi tessellation of a
564    STORM image assigns a Voronoi polygon to each localization, such that the polygon area is
565    inversely proportional to the local localization density. The spatial distribution of dynein or ORP1L
566    localizations from each ORP1L positive endolysosome is represented by a set of Voronoi
567    polygons such that smaller polygon areas correspond to regions of higher density. The Voronoi

21

568  polygons at the endolysosomal edge are extremely large and were omitted for any quantification.

569  Dynein and ORP1L clusters were segmented by grouping adjacent Voronoi polygons with areas

570  less than a selected threshold and imposing a minimum number of localizations. For mCherry-

571  ORP1L, mCherry-ORP1L-SBD, dynein (ORP1L positive endolysosomes) and dynein (ORP1L-

572  SBD positive endolysosomes), the selected area thresholds were 0.0156 $px^2$, 0.02 $px^2$, 0.01 $px^2$

573  and , 0.01 $px^2$, respectively and the minimum number of localizations imposed were16,10, 7 and

574  7, respectively. ORP1L localization density was calculated by normalizing the total number of

575  localizations per endolysosme by endolysosome area. Each endolysosme area was calculated

576  by summing up all of its Voronoi polygon areas. The low cholesterol treatment yielded

577  endolysosomes with ORP1L localization densities 4.5 times higher as compared to the high

578  cholesterol treated endoslysosome localization densities. To compare endoslysomal ORP1L

579  distribution following cholesterol treatments, the ORP1L localization densities should be

580  comparable. To address this we divided the Voronoi polygon areas of each endolysosome by its

581  mean Voronoi polygon area, such that the mean localization density of each endolysosome is in

582  reduced units of 1. All reduced Voronoi polygon areas from each endolysosme for each treatment

583  were pulled together, and the histogram was plotted.  The distribution of Voronoi areas from

584  uniformly simulated random points is fit to an analytical distribution (Tanemura, 2003).  A method

585  for calculating the KL divergence between two histograms or between a histogram and an

586  analytical distribution (Perez-Cruz, 2008) was implemented in Matlab.  The KL divergence scores

587  between the experimental reduced voronoi areas and the theoretical random distribution were

588  calculated to determine the clustering tendency score of each cholesterol treatment. All ORP1L

589  and dynein analysis has been done with endolysosmes with radius < 250nm for consistency.

590  For quantification of dynein copy numbers, the single dynein data was fit to a lognormal

591  distribution from which the μ and σ values are obtained. Using these values, the high and low

592  cholesterol dynein data is fit for the sum of convolutions of the single dynein data until a good fit

593  is obtained that does not change with fitting to higher copy number. Here, we fit until 4 dyneins.

594  Filipin intensity was calculated using Image J 'plot profile' tool. All ORP1L positive endolysosomes

595  were analyzed by drawing a line segment across it and looking at its intensity profile using the

596  'plot profile' tool. The average of 3-4 highest intensity points were taken and the average

597  background intensity was subtracted from that. For the analysis of dynein clusters on ORP1L

598  positive endolysosmal compartments, a intensity plot of the conventional ORP1L image was taken

599  and all dynein clusters falling within the Full Width Half Maxima of the profile was accepted.

600

**Acknowledgements**

**Author Contributions**

ML and ST conceived of the study. ST prepared samples, carried out experiments, wrote software and analyzed data. P.K.R. wrote software and implemented the renormalized voronoi area distribution and KL-Divergence analysis methodology. E.M.S. maintained cell lines, carried out western blot experiments, carried out all transfections, provided reagents and helped with sample preparation. M.T.G. helped carry out dilution and calibration experiments. ML wrote the manuscript, acquired funding and supervised the work. All authors provided feedback on the manuscript.

**Competing Interests:** Authors declare no competing interests.

**References**

Andronov, L., I. Orlov, Y. Lutz, J.L. Vonesch, and B.P. Klaholz. 2016. ClusterViSu, a method for clustering of protein complexes by Voronoi tessellation in super-resolution microscopy. *Sci Rep*. 6:24084.

Balint, S., I. Verdeny Vilanova, A. Sandoval Alvarez, and M. Lakadamyali. 2013. Correlative live-cell and superresolution microscopy reveals cargo transport dynamics at microtubule intersections. *Proc Natl Acad Sci U S A*. 110:3375-3380.

Bates, M., B. Huang, G.T. Dempsey, and X. Zhuang. 2007. Multicolor super-resolution imaging with photo-switchable fluorescent probes. *Science*. 317:1749-1753.

Beatty, W.L. 2006. Trafficking from CD63-positive late endocytic multivesicular bodies is essential for intracellular development of Chlamydia trachomatis. *J Cell Sci*. 119:350-359.

Belyy, V., M.A. Schlager, H. Foster, A.E. Reimer, A.P. Carter, and A. Yildiz. 2016. The mammalian dynein-dynactin complex is a strong opponent to kinesin in a tug-of-war competition. *Nat Cell Biol*. 18:1018-1024.

Brown, C.L., K.C. Maier, T. Stauber, L.M. Ginkel, L. Wordeman, I. Vernos, and T.A. Schroer. 2005. Kinesin-2 is a motor for late endosomes and lysosomes. *Traffic*. 6:1114-1124.

Cabukusta, B., and J. Neefjes. 2018. Mechanisms of lysosomal positioning and movement. *Traffic*. 19:761-769.

Cardoso, C.M., L. Groth-Pedersen, M. Hoyer-Hansen, T. Kirkegaard, E. Corcelle, J.S. Andersen, M. Jaattela, and J. Nylandsted. 2009. Depletion of kinesin 5B affects lysosomal distribution and stability and induces peri-nuclear accumulation of autophagosomes in cancer cells. *PLoS One*. 4:e4424.

Cella Zanacchi, F., C. Manzo, R. Magrassi, N.D. Derr, and M. Lakadamyali. 2019. Quantifying Protein Copy Number in Super Resolution Using an Imaging-Invariant Calibration. *Biophys J*. 116:2195-2203.

Chowdhury, S., S.A. Ketcham, T.A. Schroer, and G.C. Lander. 2015. Structural organization of the dynein-dynactin complex bound to microtubules. *Nat Struct Mol Biol*. 22:345-347.

Ehmann, N., S. van de Linde, A. Alon, D. Ljaschenko, X.Z. Keung, T. Holm, A. Rings, A. DiAntonio, S. Hallermann, U. Ashery, M. Heckmann, M. Sauer, and R.J. Kittel. 2014. Quantitative super-resolution imaging of Bruchpilot distinguishes active zone states. *Nature Communications*. 5:4650.

Elshenawy, M.M., J.T. Canty, L. Oster, L.S. Ferro, Z. Zhou, S.C. Blanchard, and A. Yildiz. 2019. Cargo adaptors regulate stepping and force generation of mammalian dynein-dynactin. *Nat Chem Biol*. 15:1093-1101.

Elshenawy, M.M., E. Kusakci, S. Volz, J. Baumbach, S.L. Bullock, and A. Yildiz. 2020. Lis1 activates dynein motility by modulating its pairing with dynactin. *Nat Cell Biol*. 22:570-578.

Encalada, S.E., L. Szpankowski, C.H. Xia, and L.S. Goldstein. 2011. Stable kinesin and dynein assemblies drive the axonal transport of mammalian prion protein vesicles. *Cell*. 144:551-565.

Ferro, L.S., S. Can, M.A. Turner, M.M. ElShenawy, and A. Yildiz. 2019. Kinesin and dynein use distinct mechanisms to bypass obstacles. *Elife*. 8.

Franke, C., U. Repnik, S. Segeletz, N. Brouilly, Y. Kalaidzidis, J.M. Verbavatz, and M. Zerial. 2019. Correlative single-molecule localization microscopy and electron tomography reveals endosome nanoscale domains. *Traffic*. 20:601-617.

Friedman, J.R., J.R. Dibenedetto, M. West, A.A. Rowland, and G.K. Voeltz. 2013. Endoplasmic reticulum-endosome contact increases as endosomes traffic and mature. *Mol Biol Cell*. 24:1030-1040.

Fu, M.M., and E.L. Holzbaur. 2014. Integrated regulation of motor-driven organelle transport by scaffolding proteins. *Trends Cell Biol*. 24:564-574.

Fu, M.M., J.J. Nirschl, and E.L.F. Holzbaur. 2014. LC3 binding to the scaffolding protein JIP1 regulates processive dynein-driven transport of autophagosomes. *Dev Cell*. 29:577-590.

Gould, G.W., and J. Lippincott-Schwartz. 2009. New roles for endosomes: from vesicular carriers to multi-purpose platforms. *Nat Rev Mol Cell Biol*. 10:287-292.

Granger, E., G. McNee, V. Allan, and P. Woodman. 2014. The role of the cytoskeleton and molecular motors in endosomal dynamics. *Semin Cell Dev Biol*. 31:20-29.

Guardia, C.M., G.G. Farias, R. Jia, J. Pu, and J.S. Bonifacino. 2016. BORC Functions Upstream of Kinesins 1 and 3 to Coordinate Regional Movement of Lysosomes along Different Microtubule Tracks. *Cell Rep*. 17:1950-1961.

Hendricks, A.G., E. Perlson, J.L. Ross, H.W. Schroeder, 3rd, M. Tokito, and E.L. Holzbaur. 2010. Motor coordination via a tug-of-war mechanism drives bidirectional vesicle transport. *Curr Biol*. 20:697-702.

Hu, Y.B., E.B. Dammer, R.J. Ren, and G. Wang. 2015. The endosomal-lysosomal system: from acidification and cargo sorting to neurodegeneration. *Transl Neurodegener*. 4:18.

Hyttinen, J.M., M. Niittykoski, A. Salminen, and K. Kaarniranta. 2013. Maturation of autophagosomes and endosomes: a key role for Rab7. *Biochim Biophys Acta*. 1833:503-510.

681 Johansson, M., M. Lehto, K. Tanhuanpaa, T.L. Cover, and V.M. Olkkonen. 2005. The oxysterol-binding
682    protein homologue ORP1L interacts with Rab7 and alters functional properties of late endocytic
683    compartments. *Mol Biol Cell*. 16:5480-5492.

684 Johansson, M., N. Rocha, W. Zwart, I. Jordens, L. Janssen, C. Kuijl, V.M. Olkkonen, and J. Neefjes. 2007.
685    Activation of endosomal dynein motors by stepwise assembly of Rab7-RILP-p150Glued, ORP1L,
686    and the receptor betaIII spectrin. *J Cell Biol*. 176:459-471.

687 Keyomarsi, K. 1996. Synchronization of mammalian cells by Lovastatin. *Methods in Cell Science*. 18:109-
688    114.

689 Kimura, S., T. Noda, and T. Yoshimori. 2008. Dynein-dependent movement of autophagosomes mediates
690    efficient encounters with lysosomes. *Cell Struct Funct*. 33:109-122.

691 Klumperman, J., and G. Raposo. 2014. The complex ultrastructure of the endolysosomal system. *Cold*
692    *Spring Harb Perspect Biol*. 6:a016857.

693 Korolchuk, V.I., and D.C. Rubinsztein. 2011. Regulation of autophagy by lysosomal positioning. *Autophagy*.
694    7:927-928.

695 Korolchuk, V.I., S. Saiki, M. Lichtenberg, F.H. Siddiqi, E.A. Roberts, S. Imarisio, L. Jahreiss, S. Sarkar, M.
696    Futter, F.M. Menzies, C.J. O'Kane, V. Deretic, and D.C. Rubinsztein. 2011. Lysosomal positioning
697    coordinates cellular nutrient responses. *Nat Cell Biol*. 13:453-460.

698 Levet, F., E. Hosy, A. Kechkar, C. Butler, A. Beghin, D. Choquet, and J.B. Sibarita. 2015. SR-Tesseler: a
699    method to segment and quantify localization-based super-resolution microscopy data. *Nat*
700    *Methods*. 12:1065-1071.

701 Maday, S., A.E. Twelvetrees, A.J. Moughamian, and E.L. Holzbaur. 2014. Axonal transport: cargo-specific
702    mechanisms of motility and regulation. *Neuron*. 84:292-309.

703 McKenney, R.J., W. Huynh, M.E. Tanenbaum, G. Bhabha, and R.D. Vale. 2014. Activation of cytoplasmic
704    dynein motility by dynactin-cargo adapter complexes. *Science*. 345:337-341.

705 Mohan, N., E.M. Sorokina, I.V. Verdeny, A.S. Alvarez, and M. Lakadamyali. 2019. Detyrosinated
706    microtubules spatially constrain lysosomes facilitating lysosome-autophagosome fusion. *J Cell*
707    *Biol*. 218:632-643.

708 Nirschl, J.J., M.M. Magiera, J.E. Lazarus, C. Janke, and E.L. Holzbaur. 2016. alpha-Tubulin Tyrosination and
709    CLIP-170 Phosphorylation Regulate the Initiation of Dynein-Driven Transport in Neurons. *Cell Rep*.
710    14:2637-2652.

711 Olenick, M.A., and E.L.F. Holzbaur. 2019. Dynein activators and adaptors at a glance. *J Cell Sci*. 132.

712 Olkkonen, V.M., and S. Li. 2013. Oxysterol-binding proteins: sterol and phosphoinositide sensors
713    coordinating transport, signaling and metabolism. *Prog Lipid Res*. 52:529-538.

714 Perez-Cruz, F. 2008. Kullback-Leibler divergence estimation of continuous distributions. *In* IEEE
715    international symposium on information theory.

716 Pfeffer, S.R. 2001. Rab GTPases: specifying and deciphering organelle identity and function. *Trends Cell*
717    *Biol*. 11:487-491.

718 Pu, J., C.M. Guardia, T. Keren-Kaplan, and J.S. Bonifacino. 2016. Mechanisms and functions of lysosome
719    positioning. *J Cell Sci*. 129:4329-4339.

720 Puchner, E.M., J.M. Walter, R. Kasper, B. Huang, and W.A. Lim. 2013. Counting molecules in single
721    organelles with superresolution microscopy allows tracking of the endosome maturation
722    trajectory. *Proc Natl Acad Sci U S A*. 110:16015-16020.

723 Rai, A., D. Pathak, S. Thakur, S. Singh, A.K. Dubey, and R. Mallik. 2016. Dynein Clusters into Lipid
724    Microdomains on Phagosomes to Drive Rapid Transport toward Lysosomes. *Cell*. 164:722-734.

725 Reck-Peterson, S.L., W.B. Redwine, R.D. Vale, and A.P. Carter. 2018. The cytoplasmic dynein transport
726    machinery and its many cargoes. *Nat Rev Mol Cell Biol*. 19:382-398.

727 Rocha, N., C. Kuijl, R. van der Kant, L. Janssen, D. Houben, H. Janssen, W. Zwart, and J. Neefjes. 2009.
728     Cholesterol sensor ORP1L contacts the ER protein VAP to control Rab7-RILP-p150 Glued and late
729     endosome positioning. *J Cell Biol*. 185:1209-1225.
730 Rosa-Ferreira, C., and S. Munro. 2011. Arl8 and SKIP act together to link lysosomes to kinesin-1. *Dev Cell*.
731     21:1171-1178.
732 Schroeder, C.M., and R.D. Vale. 2016. Assembly and activation of dynein-dynactin by the cargo adaptor
733     protein Hook3. *J Cell Biol*. 214:309-318.
734 Soppina, V., A.K. Rai, A.J. Ramaiya, P. Barak, and R. Mallik. 2009. Tug-of-war between dissimilar teams of
735     microtubule motors regulates transport and fission of endosomes. *Proc Natl Acad Sci U S A*.
736     106:19381-19386.
737 Tanemura, M. 2003. Statistical distributions of Poisson Voronoi cells in two and three dimensions. *FORMA-
738     TOKYO*. 18:221-247.
739 Torres, S., E. Balboa, S. Zanlungo, C. Enrich, C. Garcia-Ruiz, and J.C. Fernandez-Checa. 2017. Lysosomal and
740     Mitochondrial Liaisons in Niemann-Pick Disease. *Front Physiol*. 8:982.
741 Urnavicius, L., C.K. Lau, M.M. Elshenawy, E. Morales-Rios, C. Motz, A. Yildiz, and A.P. Carter. 2018. Cryo-
742     EM shows how dynactin recruits two dyneins for faster movement. *Nature*. 554:202-206.
743 van der Kant, R., I. Zondervan, L. Janssen, and J. Neefjes. 2013. Cholesterol-binding molecules MLN64 and
744     ORP1L mark distinct late endosomes with transporters ABCA3 and NPC1. *J Lipid Res*. 54:2153-
745     2165.
746 Vanlandingham, P.A., and B.P. Ceresa. 2009. Rab7 regulates late endocytic trafficking downstream of
747     multivesicular body biogenesis and cargo sequestration. *J Biol Chem*. 284:12110-12124.
748 Verdeny-Vilanova, I., F. Wehnekamp, N. Mohan, A. Sandoval Alvarez, J.S. Borbely, J.J. Otterstrom, D.C.
749     Lamb, and M. Lakadamyali. 2017. 3D motion of vesicles along microtubules helps them to
750     circumvent obstacles in cells. *J Cell Sci*. 130:1904-1916.
751 Vihervaara, T., R.L. Uronen, G. Wohlfahrt, I. Bjorkhem, E. Ikonen, and V.M. Olkkonen. 2011. Sterol binding
752     by OSBP-related protein 1L regulates late endosome motility and function. *Cell Mol Life Sci*.
753     68:537-551.
754 Wijdeven, R.H., H. Janssen, L. Nahidiazar, L. Janssen, K. Jalink, I. Berlin, and J. Neefjes. 2016. Cholesterol
755     and ORP1L-mediated ER contact sites control autophagosome transport and fusion with the
756     endocytic pathway. *Nat Commun*. 7:11808.
757 Zanacchi, F.C., C. Manzo, A.S. Alvarez, N.D. Derr, M.F. Garcia-Parajo, and M. Lakadamyali. 2017a. A DNA
758     origami platform for quantifying protein copy number in super-resolution. *Nat Methods*. 14:789-
759     792.
760 Zanacchi, F.C., C. Manzo, A.S. Alvarez, N.D. Derr, M.F. Garcia-Parajo, and M. Lakadamyali. 2017b. A DNA
761     origami platform for quantifying protein copy number in super-resolution. *Nature Methods*.
762     14:789-792.
763 Zhao, K., and N.D. Ridgway. 2017. Oxysterol-Binding Protein-Related Protein 1L Regulates Cholesterol
764     Egress from the Endo-Lysosomal System. *Cell Rep*. 19:1807-1818.

765